Chinese Chemical Letters 37 (2026) 111508

Contents lists available at ScienceDirect

Chinese Chemical Letters

journal homepage: www.elsevier.com/locate/cclet

Anchoring Co nanoparticles in P, I-doped carbon skeleton for highly efficient potassium metal anodes

Yiting Tong[a], Wei Shi[b], Qingfeng Zhang[a,*], Zheyi Zou[a], Wei Xie[a], Jianyu Huang[a], Shuhong Xie[a,*]

[a] Key Laboratory of Low Dimensional Materials and Application Technology of Ministry of Education, School of Materials Science and Engineering, Xiangtan University, Xiangtan 411105, China
[b] Key Laboratory of the Preparation and Application of Environmentally Friendly Functional Materials (Huaihua University), College of Chemistry and Materials Engineering, Huaihua University, Huaihua 418000, China

ARTICLE INFO

Article history:
Received 17 April 2025
Revised 21 June 2025
Accepted 25 June 2025
Available online 25 June 2025

Keywords:
3D skeletons
Potassiophilic elements co-doping
Dendrite suppression
Potassium metal anodes
Long cycle life

ABSTRACT

Owing to the low redox potential and high theoretical specific capacity, potassium metal batteries (PMBs) have become one of the suitable candidates for high specific energy batteries. However, challenges including uncontrolled dendrite growth and interfacial instability severely hinder their practical applications. Herein, we develop a cobalt-anchored, phosphorus-iodine co-doped 3D carbon skeleton (PI-Co/GCNT) that synergistically integrates heteroatom co-doping effects and structural engineering to address these limitations. Experiments reveal that the doping of P and I induces charge redistribution on the Co/GCNT, which collectively enhances the K^+ adsorption energy compared to Co/GCNT and GCNT. This strategy creates abundant potassiophilic sites that reduce nucleation overpotential (14 mV) and inhibit dendrite growth. The 3D porous architecture not only accommodates volume fluctuations but also ensures rapid ion transport through low-tortuosity channels. The assembled K-PI-Co/GCNT symmetrical cells keep cycling over 1000 h at 1 mA/cm^2 with a low polarization of 40 mV. Paired with organic cathodes (PTCDA), the K-PI-Co/GCNT anode delivers superior cycle and rate performance compared to the bare K in full cells. This work elucidates the critical role of heteroatom co-doping for dendrite-free anodes, providing a universal design paradigm for alkali metal batteries.

© 2026 Published by Elsevier B.V. on behalf of Chinese Chemical Society and Institute of Materia Medica, Chinese Academy of Medical Sciences.

Owing to the abundance of potassium resources and the same working mechanism as lithium-based energy storage systems, the research on potassium-based energy storage systems is attracting intensive interest [1–3]. Various anode materials have been applied to potassium-ion batteries (PIBs), including carbon materials [4,5], metal oxides/sulfides/selenides/phosphides [6–9], alloys [10,11], and K metal [12]. Among these anode materials, potassium-metal anodes (PMAs) are expected to be a reliable choice matching the increasing demand for energy storage, owing to the lowest redox potential (−2.93 V *vs.* standard hydrogen electrode) and high specific capacity (687 mAh/g) [12]. On this basis, the PMAs would be applied to the advanced high-energy systems such as K-O_2 [13] and K-S [14] systems, fulfilling the necessity for low-cost and high-energy density batteries. Unfortunately, the uneven deposition of K-metal leads to undesirable potassium dendrites growth easily. Accompanying volumetric variations can break the vulnerable SEI and cause more side-reactions between the fresh K-metal and electrolyte, consuming more K^+ and leading to horrible K-metal dendrites [12]. Consequently, it is necessary to achieve stable K deposition/dissolution in an operating battery.

As the research on PMAs advances, several methods have been exploited to address the problems mentioned above. Such as optimizing the composition of electrolytes [15], constructing a 3D skeleton [16], designing artificial SEI layers [17] and applying the solid-state electrolytes [18]. Among these methods, constructing a 3D K-composite skeleton is an ideal choice. Firstly, a suitable 3D framework could accommodate the volume change caused by K dendrites during cycling. Besides, distributing abundant and even active absorption sites in the 3D skeleton is useful to enable uniform distribution of current density, which is beneficial to restrain the K dendrites growth. Researchers mostly choose carbon materials and metal materials as 3D skeletons. Compared to metals, carbon materials exhibit high electrical conductivity, excellent mechanical strength and flexibility. Recently, the carbon nanotube (CNT), biomass-derived carbon materials, carbon nanofiber and reduced graphene oxide (rGO) have been researched as effec-

* Corresponding authors.
E-mail addresses: zhangqf@xtu.edu.cn (Q. Zhang), shxie@xtu.edu.cn (S. Xie).

https://doi.org/10.1016/j.cclet.2025.111508
1001-8417/© 2026 Published by Elsevier B.V. on behalf of Chinese Chemical Society and Institute of Materia Medica, Chinese Academy of Medical Sciences.

tive hosts to accommodate the K deposition. However, rGO sheets are easily stacked with each other, CNT tends to aggregate. Besides, K metal tends to deposit on the fully dense rGO sheets, due to the complete and stacked rGO sheets possess highly tortuosity and long ions transport paths, thereby causing K dendrites. Research shows that it is helpful to disperse the CNT inside the rGO sheets, thereby suppressing the stacking/aggregation of rGO and CNT [19]. But only focusing on designing the host framework would be an inadequate method for suppressing the growth of K metal dendrite. Introducing potassiophilic sites into 3D host has recently drawn great attention. For instance, studies show that the heteroatom-doping can help to increase the binding energy with K ions, such as B-, N-, and P-doping. Loading potassiophilic metal nanoparticles in the 3D host can also improve the affinity with K ions, such as Ag, Co, Sb, have been used as potassiophilic sites to modify the host [20]. With synergistic effects of morphological and structural, the potassiophilic 3D skeleton adjusts the internal electric field, homogenizes the current density and K deposition, thus limiting K dendrite growth and obtaining a stable K-metal anode.

Herein, we proposed a porous 3D rGO–CNT composite film with Co-anchored P, I co-doped as the 3D host (PI-Co/GCNT). The CNT dispersed into the porous rGO layers uniformly, shortening the K ions transport paths. More importantly, by modifying with the Co nanoparticles and doping with P, I heteroatoms, the PI-Co/GCNT host exhibit great affinity to K ions, the potassiophilic feature provides strong interaction with K^+ that leads to uniform K deposition and great cycling stability. Benefiting from the potassiophilic elements and 3D porous skeleton, a durable K-metal anode was developed. The symmetric cell with K-PI-Co/GCNT anode exhibits extraordinary K metal plating/stripping ability, showing an average coulombic efficiency of 97.5 % and a cycle stability close to 500 cycles at 1 mA/cm^2. And K-PI-Co/GCNT anode maintains an excellent cycling performance for 1000 h at a current density of 1 mA/cm^2 and an areal capacity of 1 mAh/cm^2. Furthermore, the full cell paired with K-PI-Co/GCNT anode also possesses a significantly improved long-term cycling performance at a 1000 mA/g and better rate performance than a bare K anode.

The preparation of PI-Co/GCNT is shown in Fig. 1a, involving a simple chemical bath deposition. The process includes adding the Co^{2+} suspension to the GO and CNT mixed suspension, followed by dropwise addition of $NH_3{\cdot}H_2O$ solution to adjust the pH. The suspension was filtered, and then calcination was performed to obtain the Co/GCNT film. During calcination, CoO was reduced to Co particles *via* carbothermic reduction. Phosphorous triiodide (PI_3) was vaporized and condensed to uniformly absorption on the surface and interlayer of film. Finally, phosphorus-iodine co-doped (PI-Co/GCNT) films with good bending properties were obtained using ethylene glycol (Figs. S1a-c in Supporting information). The morphology of PI-Co/GCNT was obtained by scanning electron microscope (SEM). As illustrated in Figs. 1b and c, the Co nanoparticles are distributed on the rGO sheets evenly. The thickness of the PI-Co/GCNT film is ≈20 μm, and PI-Co/GCNT film exhibits a 3D loose layer-like structure (Figs. S2a and b in Supporting information). Compared with GCNT films (Figs. S3a and b in Supporting information) and Co/GCNT (Figs. S3c and d in Supporting information), the PI-Co/GCNT film demonstrates rationally distributed in-plane pores and potassiophilic sites, which endow the composite with enhanced structural stability. This 3D porous skeleton can not only suppress the stacking of rGO but also provide channels for rapid and continuous ions transportation. The CNT inside homogenizes electronic distribution among rGO, thus homogenizing the current density of the electrode and K plating. The increased space also assures good penetration of electrolyte and provides ample space for K storage [21]. The energy dispersive spectroscopy (EDS) mapping of film surface (Fig. S4 in Supporting information) and cross section (Fig. 1d) indicate that P, I and Co are distributed uniformly between layers as well. The doping of Co, P and I could offer uniformly potassiophilic sites to facilitate nucleation of K metal. As shown in Fig. 1e, the atomic force microscopy (AFM) test was performed to study the morphology of PI-Co/GCNT surface, which exhibits relatively high flatness. According to the X-ray diffraction (XRD) pattern in Fig. 1f, the peaks at 2θ of 21.2° and 26.2° indicates the reduction of GO and the existence of CNT [22]. The peak at 2θ of 26.2° is indexed to the (002) diffraction planes of a typical graphitic carbon peak. After the heating treatment and exposure to PI_3 vapor, no obvious shift is observed in the peaks of PI-Co/GCNT, indicating the good stability of the structure. Heteroatoms doping could affect the crystal structure properties of the material. The enhancement of the intensity of (002) peaks may be attributed to the doping of P, I atoms, repairing the defects generated in the carbon lattice [23]. Due to the low cobalt content, the diffraction peaks of Co show weak signals at 44.2°, 51.5°, which correspond to the (111) and (200) to diffraction planes of Co metal (JCPDS No. 15–0806), respectively. Fig. 1g shows the Raman spectra of GCNT, Co/GCNT and PI-Co/GCNT, the D band (peak at 1348.32 cm^{-1}) corresponds to the disordered graphite caused by defects and G band (peak at 1596.8 cm^{-1}) attributes to graphitization. The Co/GCNT (I_D/I_G = 1.14) and PI-Co/GCNT (I_D/I_G = 1.08) shows highly disordered, indicating abundant defects. The I_D/I_G of PI-Co/GCNT is slightly lower than that of Co/GCNT, which may be due to the doping of P and I. Correspondingly, PI-Co/GCNT shows an appropriate specific surface area (99.03 m^2/g) comparing with GCNT and Co/GCNT in Fig. S5a (Supporting information). The structural defects were effectively repaired dual-element doping of P and I, leading to a reduction in the specific surface area of PI-Co/GCNT. PI-Co/GCNT exhibits an average pore size between 2.1 nm and 3.8 nm, and the active sites provided by defects/edges contribute to the uniformly distributed K^+ current density and promote the penetration of electrolytes (Fig. S5b in Supporting information).

The morphology of PI-Co/GCNT film is further characterized by transmission electron microscope (TEM). In Fig. 2a, it can be observed that the Co nanoparticles and CNT are dispersed homogenously. The pink circles next to the Co nanoparticles represent the holes caused by carbothermic reduction. Fig. 2b shows the TEM image of a single Co nanoparticle, Figs. 2c and d correspond to two different areas of it. In Fig. 2c, the lattice fringe of Co nanoparticle with 0.203 nm interval corresponds to the (111) facets of Co. The more apparent lattice fringe in Fig. 2d corresponds to the (002) facets of CNT. Additionally, Figs. S6a and b (Supporting information) further substantiate the existence of holes, CNT and Co nanoparticles. According to the EDS (Fig. 2e), the distribution of Co, P and I is uniform, and there are no obvious P or I particles. The X-ray photoelectron spectroscopy (XPS) survey spectrum shows the distinct signals of C, O, Co, P and I (Fig. S7a in Supporting information). The XPS spectrum of C 1s (Fig. 2f) shows that four peaks at 284.05, 284.8, 285.65, and 287.05 eV are assigned to C-P, C–C, C–O-P/C–O/C-I and C=O, respectively, indicating the covalent incorporation of heteroatoms (P, I) into the carbon lattice. Notably, Co 2p (Fig. 2g) exhibits a positive shift in binding energy compared to Co/GCNT (Fig. S8c in Supporting information), suggesting electron transfer from Co to electronegative iodine dopants [24]. This electronic coupling between metallic Co and I atoms modulates the local charge environment, potentially enhancing interfacial reactivity toward K adsorption. The coexistence of Co^0 (779.16/793.83 eV) and Co-O/Co-C species (782.63/798.31 eV, 785.32/801.11 eV) further demonstrates the stabilized coordination states of Co nanoparticles. Crucially, the P 2p spectrum (Fig. 2h) and I 3d spectrum (Fig. 2i) provide direct evidence of heteroatom-induced charge redistribution. The dominant P-C bond (134.25 eV) and residual P-O bond (135.25 eV) confirm phosphorus integration into the carbon framework. For iodine species, the peaks at 618.62 eV (C-I$^+$-C) and

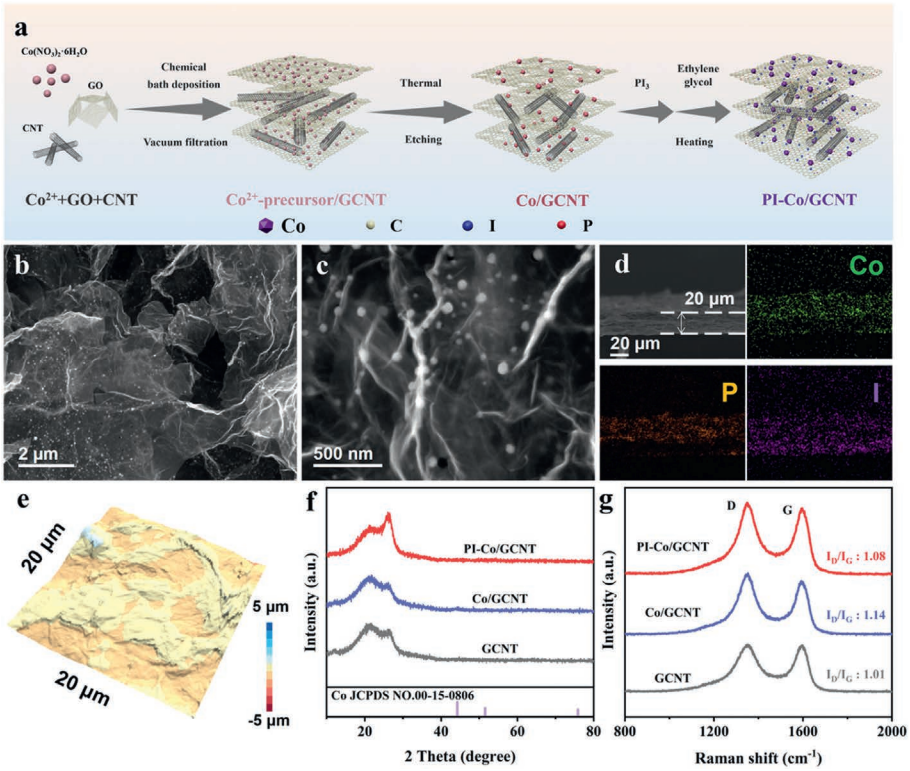


Fig. 1. (a) A synthetic diagram of PI-Co/GCNT. (b, c) SEM images of PI-Co/GCNT film. (d) Cross-sectional SEM image and EDS mappings of a PI-Co/GCNT film. (e) 3D AFM image of PI-Co/GCNT film surface. (f) XRD patterns and (g) Raman spectra of GCNT, Co/GCNT and PI-Co/GCNT.

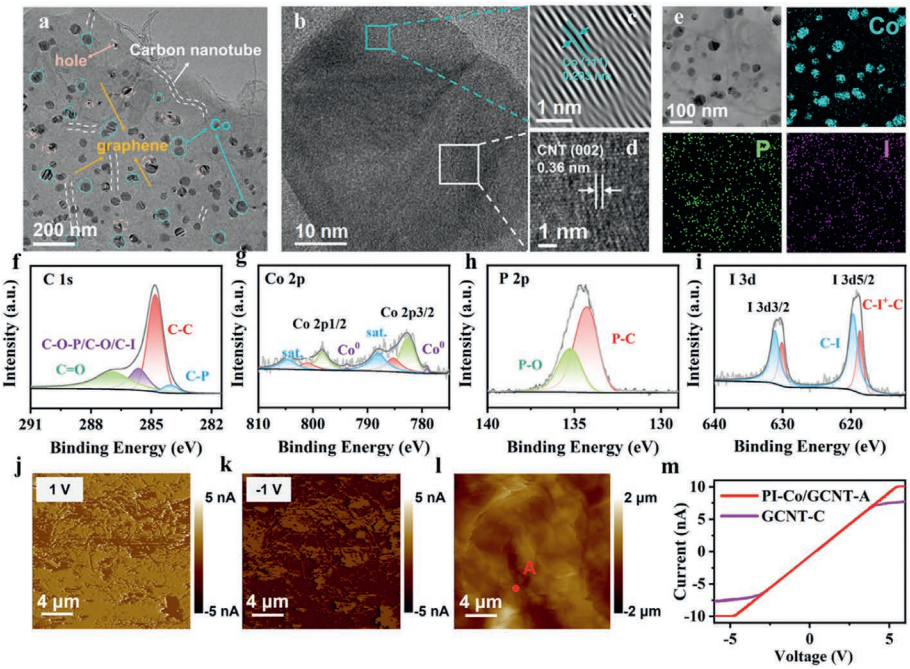


Fig. 2. (a) TEM image of PI-Co/GCNT. (b-d) HRTEM images of PI-Co/GCNT. (e) TEM image and EDS mappings of PI-Co/GCNT. XPS spectra of (f) C 1s, (g) Co 2p, (h) P 2p, (i) I 3d. Conductive-AFM results of PI-Co/GCNT film performed at (j) +1 V and (k) −1 V, respectively. (l) AFM image of PI-Co/GCNT film. (m) Current–voltage spectroscopy curves conducted at two different sample positions marked by PI-Co/GCNT-A (red curve) and GCNT-C (purple curve).

619.6 eV (C-I) indicate the doping of I. As reported [25,26], these synergistic effects shows stronger K^+ adsorption. With a 500 MΩ resistor in series, conductive-atomic force microscopy (C-AFM) was used to evaluate the conductivity of PI-Co/GCNT film, at sample potentials of $V_{sp} = +1.0$ V (Fig. 2j) and $V_{sp} = -1.0$ V (Fig. 2k). The C-AFM test results of GCNT film are shown in Figs. S9a and b (Supporting information). It can be observed that both the GCNT 3D skeleton and PI-Co/GCNT show good conductivity. Single spots of the samples were chosen randomly to further compare their current–voltage (*I–V*) spectroscopy curves, which are marked by PI-Co/GCNT-A in Fig. 2l and GCNT-C in Fig. S9c (Supporting information). In Fig. 2m, the current and voltage are linearly related, show-

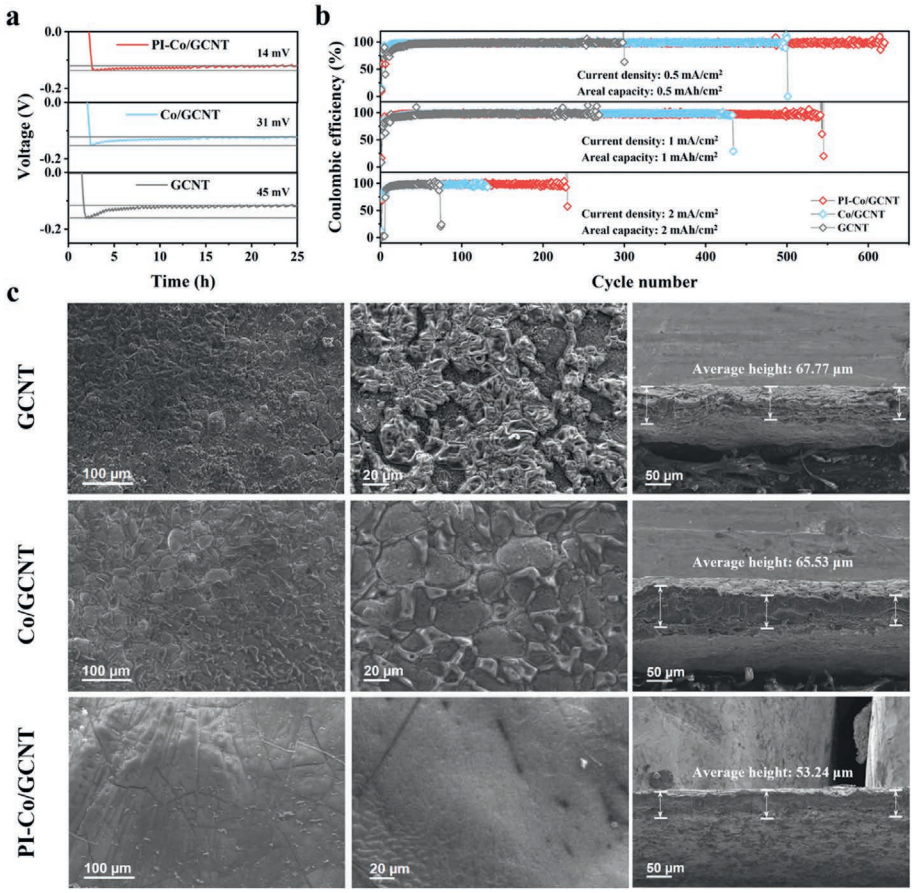


Fig. 3. (a) Nucleation overpotential profiles of K deposition on GCNT, Co/GCNT, and PI-Co/GCNT. (b) Coulombic efficiency of K plating/stripping on GCNT, Co/GCNT, and PI-Co/GCNT at different current densities (0.5, 1, 2 mA/cm^2). (c) SEM images of K deposition morphologies and corresponding cross-sectional view on GCNT, Co/GCNT, and PI-Co/GCNT after plating capacity of 5 mAh/cm^2.

ing high conductivity. However, it is apparent that the PI-Co/GCNT has a larger current range under the same condition, implying better conductivity.

To identify the initial K nucleation behavior on different films, the voltage-time-profiles of GCNT, Co/GCNT, PI-Co/GCNT when discharging at 0.2 mA/cm^2 for 25 h with 4 mol/L KFSI in DME were recorded. In the voltage-time profile, the difference between the lowest voltage point and the following plateau is nucleation overpotential [16]. As shown in Fig. 3a, due to the low-tortuosity porous skeleton and the doping of potassiophilic elements, the K nucleation overpotential of PI-Co/GCNT ($\Delta V_{\text{PI-Co/GCNT}}$) is around 14 mV. The value is smaller than that of the GCNT ($\Delta V_{\text{GCNT}} = 45$ mV) and Co/GCNT ($\Delta V_{\text{Co/GCNT}} = 31$ mV), indicating that the synergistic electronic effects between Co, P and I enhances the K host's potassiophilicity effectively, further reducing the nucleation energy barrier of K and offering a faster diffusion rate of K ions. Coulombic efficiency (CE) can demonstrate electrochemical stability of K metal hosts upon repeated cycles, and it is defined as the ratio of K stripping capacity to plating capacity. Fig. 3b and Fig. S10 (Supporting information) show the CE performance of GCNT, Co/GCNT, PI-Co/GCNT when cycling at 0.5, 1 and 2 mA/cm^2. rGO–CNT-based carbon matrix exhibits good CE performance. But in comparison, K-GCNT shows the worst K plating/stripping behavior, which may be due to the fully dense GO presenting long transport paths for K ions. By the etching of graphene and modifying of Co, the transport of K ions is more rapidly and easily, thereby homogenizing the current density. The K-Co/GCNT shows a better performance (490 cycles at 0.5 mA/cm^2). While K-PI-Co/GCNT presents excellent cycle stability at 0.5 mA/cm^2 with an average CE of 97.75 % over 610 cycles. At high current densities (1 and 2 mA/cm^2), K-PI-Co/GCNT operates for about 500 cycles and 200 cycles respectively. Besides, in Fig. S11, the CE of PI-Co/GCNT maintains stable when increasing the current density and areal capacity, showing good K metal plating/stripping ability. After plating 5 mAh/cm^2, the morphology of initial K deposition on GCNT, Co/GCNT, PI-Co/GCNT were examined by SEM (Fig. 3c). The plated K on GCNT is loosened and rough with visible K dendrites. Furthermore, the uneven K deposition causes some holes in the deposition surface (Fig. S12a in Supporting information). In comparison, although the morphology of initial K deposition on Co/GCNT is relatively denser, visible K dendrites and holes are still present on the surface, as illustrated in Fig. S12b (Supporting information). The irregularly shaped dendrites are likely to puncture the separator and accelerate battery failure [27]. On the PI-Co/GCNT substrate, both the top surface and cross section are denser and smoother (Fig. S12c in Supporting information). When depositing for the same time, the thickness of K-PI-Co/GCNT is thinner than that of K-GCNT and K-Co/GCNT, suggesting that the K dendrite growth is significantly inhibited and the volume change caused by K dendrites during plating can be accommodated by the inner space of PI-Co/GCNT. The synergistic effects of 3D porous skeleton and potassiophilic elements doping are expected to produce a rapid K ions transport and a homogeneous electrode current density, regulating the evenly deposition of K and suppressing the K dendrites.

As illustrated in Fig. 4a, with plating time increasing, star-like dendrites grew radially in the K plating process (10 min), thus easily causing bare K to a short-circuit. In contrast, there were no potassium dendrites in the K-PI-Co/GCNT. These results demon-

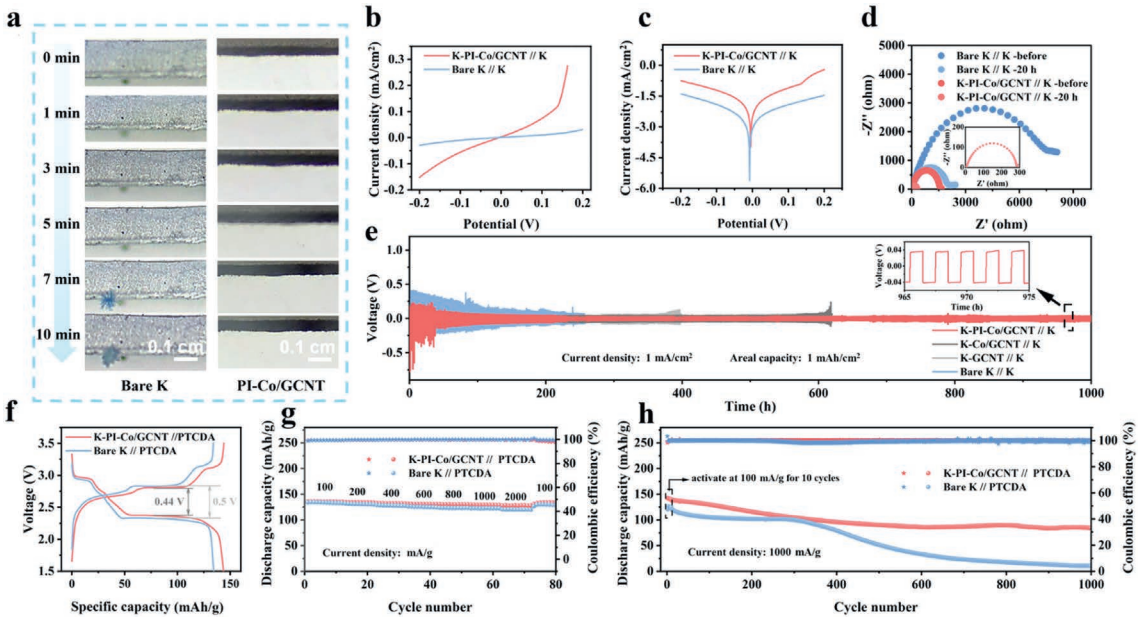


Fig. 4. (a) *In situ* optical microscopy images of K plating on bare K and PI-Co/GCNT electrodes at 5 mA/cm^2. (b) Linear sweep voltammetry (LSV) and (c) Tafel curve of bare K and K-PI-Co/GCNT symmetric cell. (d) EIS of bare K and K-PI-Co/GCNT symmetric cell before and after cycling for 20 h. (e) Comparison of the cycle stability of the symmetric cells at 1 mA/cm^2 with an areal capacity of 1 mAh/cm^2. (f) Charge/discharge curves 100 mA/g of bare K//PTCDA and K-PI-Co/GCNT//PTCDA. (g) Rate performance of bare K//PTCDA and K-PI-Co/GCNT//PTCDA at different current densities of 100–2000 mA/g. (h) The cycling performances of bare K//PTCDA and K-PI-Co/GCNT//PTCDA at 1000 mA/g.

strate that the growth of potassium dendrites could be regulated by the porous 3D skeleton and potassiophilic sites effectively, thereby ensuring the stable cycling of K-PI-Co/GCNT. The linear sweep voltammetry (LSV) and the Tafel plot were tested to study the ions diffusion kinetics at the interface. As shown in Fig. 4b, the slope of K-PI-Co/GCNT is more drastic than that of bare K. In Fig. 4c, the exchange current density (i_0) was obtained through an extrapolation procedure according to the tafel plots. The i_0 of the K-PI-Co/GCNT is 1.3×10^{-2} mA/cm^2, whereas the i_0 of bare K is 2.24×10^{-3} mA/cm^2, indicating that the K^+ plating/stripping processing is more facile for K-PI-Co/GCNT. Fig. 4d shows the Nyquist plot of the symmetric cells before and after cycling. After cycling for 20 h, the interfacial impedance decreases. It is evident that the interfacial impedance of K-PI-Co/GCNT before and after cycling is lower than that of bare K, indicating a more stable interface. The long-term cycling stability of bare K and K-PI-Co/GCNT was evaluated in a symmetric cell (Fig. 4e). When operating at a current density of 1 mA/cm^2@1 mAh/cm^2, the K-PI-Co/GCNT operated over 1000 h with a stable overpotential of 40 mV, demonstrating excellent symmetric battery cycling performance compared to potassium-metal anode reported in other studies (Table S1 in Supporting information). The initial polarization voltage of K-PI-Co/GCNT symmetric cell is high and then decreases to maintain stability, probably due to the requirement to overcome a nucleation energy barrier during the initial process and subsequently establish a stable mass transfer plateau [28]. The K-GCNT and K-Co/GCNT anodes exhibited failure after cycling about 400 and 600 h, respectively, whereas the bare K performs a short cycle life for only 257 h. As shown in Fig. S13 (Supporting information), PI-Co/GCNT shows better wettability (7.3°) with the electrolyte. The improved wettability ensures a uniform SEI layer, thus homogenizing the K^+ flux and achieving long cycle life. To study the difference of K plating/stripping morphology on different films, the SEM results of the anodes after cycling for 20 h at 1 mA/cm^2@1 mAh/cm^2 are shown in Fig. S14 (Supporting information). The surface of K-GCNT is rougher than K-Co/GCNT and K-PI-Co/GCNT (Figs. S14a and d). Although the surface of K-Co/GCNT is relatively smoother, it still exhibits undulations (Figs. S14b and e). The uneven areas tend to initiate potassium dendrites. Surprisingly, the K-PI-Co/GCNT displays a flat and dendrite-free K morphology (Figs. S14c and f), indicating that the synergistic effects of 3D porous skeleton and potassiophilic activation sites (Co, P, I) are effective. The K-PI-Co/GCNT also performed superiority than bare K, K-GCNT and K-Co/GCNT when cycling at different current densities and areal capacities of 0.2 mA/cm^2@0.2 mAh/cm^2, 2 mA/cm^2@2 mAh/cm^2 and 4 mA/cm^2@4 mAh/cm^2 (Figs. S15-S17 in Supporting information). Fig. S18 (Supporting information) shows the rate performance of K-PI-Co/GCNT and bare K from 0.1 mA/cm^2 to 4.0 mA/cm^2. The bare K anode shows a short-circuit at 3 mA/cm^2. However, K-PI-Co/GCNT shows good reversibility, indicating the loose and potassiophilic layer-like structure plays a positive role in K ions transport. When the current density returns to 0.1 mA/cm^2, the overpotential of K-PI-Co/GCNT is lower than initial, it can be attributed to the formation of uniform SEI layer.

To verify the practical applications of the K-PI-Co/GCNT anode, a full cell is assembled with an organic cathode (PTCDA). Cyclic voltammetry (CV) test was conducted (Fig. S19 in Supporting information). The K-PI-Co/GCNT anode shows better reversibility and stability than bare K. Moreover, the CV profiles of the K-PI-Co/GCNT anode approximately overlaps except for the first cycle, implying its excellent cycle performance. The charging/discharging curves at 100 mA/g in Fig. 4f show that the polarization voltage of K-PI-Co/GCNT//PTCDA (0.44 V) is lower than that of bare K//PTCDA (0.5 V), indicating that the cell with K-PI-Co/GCNT anode possesses a faster kinetics of the redox reaction. Fig. 4g is the rate capability of full cells, when the current density changes from 100 mA/g to 2000 mA/g, the capacity retention rate of K-PI-Co/GCNT//PTCDA full cell keeps about 94.4 %, which is higher than the cell with bare K anode of 89.2 %, indicating the K-PI-Co/GCNT anode shows a better rate performance. Additionally, it should be noted that the K-PI-Co/GCNT//PTCDA full cell also possesses lower voltage polarization than bare K//PTCDA (Fig. S20 in Supporting information). At 100 mA/g, K-PI-Co/GCNT//PTCDA full cell keeps an initial discharge

specific capacity of ≈143.67 mAh/g with a good retention rate of 95 % after 100 cycles (Fig. S21 in Supporting information). The interfacial resistance of K-PI-Co/GCNT//PTCDA full cell is smaller than the cell with bare K anode after cycling at 100 mA/g (Fig. S22 in Supporting information), which is associated with the formation of uniform SEI layer and the K stable plating/stripping process. As shown in Fig. 4h, K-PI-Co/GCNT//PTCDA maintains a capacity of 84.3 mAh/g at 1000 mA/g after 1000 cycles. However, the capacity of the bare K decays from 124.82 mAh/g to 10.31 mA/g, further demonstrating that the potassiophilic 3D skeleton (K-PI-Co/GCNT) exhibits the ability to rapidly transmit K^+, leading to better cycling performance.

We presented an effective method to improve the electrochemical performances of K metal anode *via* constructing a stable potassiophilic 3D skeleton host. Results show that the porous rGO–CNT is favorable to accommodate K-metal and facilitate homogenized K^+ flux and rapid K^+ transport. Accompanying with the modifying of Co nanoparticles and the doping of P, I elements, the potassiophilicity of this 3D host is greatly improved. The potassiophilic materials are distributed uniformly inside the 3D host, regulating the nucleation and deposition, and accelerating the transport kinetics that benefit from the strong affinity with K^+. The PI-Co/GCNT anode shows long lifespan and lower voltage polarization, keeping 40 mV voltage polarization after cycling for 1000 h at 1 mA/cm^2@1 mAh/cm^2. When paired with the PTCDA as the cathode, K-PI-Co/GCNT//PTCDA full cell delivers a discharge specific capacity of 84.3 mAh/g at 1000 mA/g, exhibiting better electrochemical performance than that of bare K//PTCDA. The design of appropriate 3D host and choices of potassiophilic elements provide an effective method to effectively regulate the K dendrite, maintain uniform K plating, and offer some light for developing the high-power-density and dendrite-free K anodes.

CRediT authorship contribution statement

Yiting Tong: Writing – original draft, Visualization, Methodology, Investigation, Data curation, Conceptualization. **Wei Shi:** Investigation, Data curation. **Qingfeng Zhang:** Writing – review & editing, Project administration, Methodology, Investigation, Funding acquisition, Conceptualization. **Zheyi Zou:** Visualization, Methodology, Investigation. **Wei Xie:** Data curation. **Jianyu Huang:** Writing – review & editing, Resources. **Shuhong Xie:** Writing – review & editing, Supervision, Resources.

Declaration of competing interest

The authors declare that they have no known competing financial interests or personal relationships that could have appeared to influence the work reported in this paper.

Acknowledgments

This work was financially supported by the National Natural Science Foundation of China (Nos. 52202308, U20A20336, 21935009), Natural Science Foundation of Hebei Province (No. B2024203054).

Supplementary materials

Supplementary material associated with this article can be found, in the online version, at doi:10.1016/j.cclet.2025.111508.

References

[1] Z. Yu, Y. Xie, B. Xie, et al., Energy Storage Mater. 25 (2020) 416–425.
[2] W. Liu, W. Liu, Y. Jiang, et al., Chin. Chem. Lett. 32 (2021) 1299–1308.
[3] Y. Tan, F. Mo, H. Li, Nano-Micro Lett. 17 (2025) 126.
[4] Q. Zhang, X. Cheng, C. Wang, et al., Energy Env. Sci. 14 (2021) 965–974.
[5] X. Liu, T. Ji, H. Guo, et al., Electrochem. Energy R 5 (2022) 401–433.
[6] W. Li, Q. Zhang, Q. Pei, et al., Adv. Funct. Mater. 34 (2024) 2404197.
[7] Q. Chen, H. Li, H. Li, et al., Chin. Chem. Lett. 34 (2023) 107402.
[8] Y. Wei, W. Hou, P. Zhang, et al., Chin. Chem. Lett. 33 (2022) 3212–3216.
[9] Z. Chen, Y. Wu, X. Liu, et al., J. Energy Chem. 81 (2023) 462–471.
[10] Z. Chen, H. Lin, Y. Tan, et al., Adv. Funct. Mater. 34 (2024) 2407653.
[11] H. Huang, J. Wang, X. Yang, et al., Angew. Chem. Int. Ed 59 (2020) 14504–14510.
[12] C. Wei, Y. Tao, H. Fei, et al., Energy Storage Mater. 30 (2020) 206–227.
[13] D.C. Kong, M. Avdeev, L.N. Song, et al., Energy Storage Mater. 72 (2024) 103699.
[14] W. Song, X. Yang, T. Zhang, et al., Nat. Commun. 15 (2024) 1005.
[15] D. Wang, Z. Wang, D. Zhai, et al., Small 20 (2024) e2403642.
[16] S. Xie, W. Xie, Q. Zhang, et al., Adv. Funct. Mater. 33 (2023) 2302880.
[17] H. Ding, J. Wang, J. Zhou, et al., Nat. Commun. 14 (2023) 2305.
[18] Z. Lu, P. Qiu, J.X. Kang, et al., ACS. Appl. Mater. Interfaces 16 (2024) 10070–10077.
[19] X.L. Li, S. Huang, D. Yan, et al., Energy Env. Mater. 6 (2022) e12274 6.
[20] S. Baek, T. Jung, S. Jie, et al., Int. J. Energ. Res. 52 (2023) 6680001.
[21] Y. Feng, A.M. Rao, J. Zhou, et al., Adv. Mater. 35 (2023) e2300886.
[22] L. Stobinski, B. Lesiak, A. Malolepszy, et al., J. Electron. Spectrosc. 195 (2014) 145–154.
[23] X. Mu, B. Yuan, X. Feng, et al., RSC Adv. 6 (2016) 105021–105029.
[24] L.K. Zhao, X.W. Gao, J. Mu, et al., Adv. Funct. Mater. 33 (2023) 202304292.
[25] J. Liu, D. Wang, K. Huang, et al., ACS Nano 15 (2021) 18125–18134.
[26] H. Yang, F. He, F. Liu, et al., Adv. Mater. 36 (2024) e2306512.
[27] T. Ji, X. Liu, T. Zhang, et al., Adv. Energy Mater. 14 (2024) 2401908.
[28] X. Xie, L. Deng, L. Li, et al., Energy Storage Mater. 73 (2024) 103834.